Journal of The Electrochemical Society, **161** (8) E3028-E3035 (2014)
0013-4651/2014/161(8)/E3028/8/$31.00 © The Electrochemical Society

JES Focus Issue on Mathematical Modeling of Electrochemical Systems at Multiple Scales

Impact of the Cathode Microstructure on the Discharge Performance of Lithium Air Batteries: A Multiscale Model

Kan-Hao Xue,[a,b] Trong-Khoa Nguyen,[a,b] and Alejandro A. Franco[a,b,*,z]

[a]*Laboratoire de Réactivité et Chimie des Solides, UMR CNRS 7314, Université de Picardie Jules Verne, Amiens Cedex 80039, France*
[b]*Réseau sur le Stockage Electrochimique de l'Energie (RS2E), FR CNRS 3459, Amiens Cedex 80039, France*

A multiscale model of lithium air batteries considering cathode pore size distribution is proposed, where the morphology of the discharge product, Li_2O_2, is assumed to be thin films covering the surface of the pores. In the model, active surface area degrades during discharge because of three reasons. First, the effective radius of pores decreases due to Li_2O_2 coverage. Secondly, small pores may be fully choked. Thirdly, thick Li_2O_2 film may block the electron tunneling process, rendering the surface inactive. Simulation results reveal that the end of discharge in cells made of Super P and Ketjen Black carbons is caused by unavailable surface area near the air inlet, rather than the full choking of pores. Larger discharge capacity is found in the Ketjen Black cell because its high specific surface area leads to slower Li_2O_2 thickness growth rate. We compare this tunneling-limited model with a linear resistance model where the Li_2O_2 thin film resistance is assumed to be proportional to its thickness. Different shapes of discharge curves have been discovered: the former has a long discharge plateau followed by a sudden drop of cell voltage, while the latter shows a gradual decrease of cell voltage. These results are discussed in relation to the experimental knowledge.

Manuscript submitted January 30, 2014; revised manuscript received February 17, 2014. Published March 7, 2014. *This paper is part of the JES Focus Issue on Mathematical Modeling of Electrochemical Systems at Multiple Scales.*

Lithium air battery (LAB) has attracted much attention during the last years due to its high energy density.[1] Yet, it is widely accepted that many obstacles must be overcome in order to realize practical LABs.[2] For non-aqueous LABs, the challenges include searching for a proper cathode material with proper solvents,[3] stabilizing the electrolyte/anode interface,[4] optimization of the cathode structure and morphology,[5–9] etc. The focus of cathode material research has evolved from the use of carbon, to nanoporous gold[10] or platinum-gold,[11] and more recently further to compounds like TiC.[12] Carbon suffers from instability upon high voltage charging above 3.5 V,[13] while nanoporous gold may circumvent this problem. Recently, Bruce's group[12] reported that it is possible to use TiC cathode with DMSO solvent to achieve the same or even better performance than nanoporous gold, while the specific energy density of TiC is much higher than nanoporous gold, not to mention the much lower material cost of TiC. In addition, some stable solvents have been identified, such as DMSO[10,14] and DMA.[15] They generally lead to Li_2O_2 production and consumption in long term cycling, without generating Li_2CO_3. These findings have greatly pushed forward the non-aqueous LAB technology, but it also deserves to notice that the optimization of the cathode structure, characterized by its specific surface area and pore size distribution (PSD) but not the material used, is also an important aspect to be considered for developing efficient LABs.

Aside from experimental methods, physical modeling affords useful insights into the operation principles of electrochemical power generators.[16–20] As discussed by us in a recent review paper,[21] there are several works published reporting the continuum-scale modeling of the LABs.[22–27] Nevertheless, the detailed PSD in the cathode is usually not considered, except for the work of Nimon et al.,[27] who considered the Li_2O_2 precipitation in various sizes of pores using the so-called Kelvin approach. Within this approach, whether Li_2O_2 prefers to precipitate in small or large pores depends on the relative surface energy of electrolyte/pore-wall interface ($\gamma_{E,W}$) compared with discharge product/pore-wall interface ($\gamma_{Li_2O_2,W}$). If $\gamma_{E,W}$ is higher, Li_2O_2 tends to precipitate in large pores, otherwise it prefers to precipitate in small pores. However, in the surface-limited reaction case, Li_2O_2 seems to precipitate locally, regardless of the surface curvature, because of its extremely low solubility in organic solvents. In addition, the past modeling approaches did not differentiate between various oxygen reduction reaction (ORR) mechanisms. In reality both surface-limited reaction and solution phase reaction can occur. In the former case the reaction requires surface adsorption such that a thin Li_2O_2 film is supposed to cover the active electrode surface,[28,29] where the insulating nature of Li_2O_2 may cause electrical passivation. In the latter case O_2^- is relatively stable in the solution such that Li_2O_2 is crystallized in the solution.[30] Recently, Mitchell et al.[31] and Adams et al.[32] reported that the morphology of Li_2O_2 in LAB strongly depends on the discharge current density. In Adams et al.'s work, at low rates below 0.025 mA/cm^2 the Li_2O_2 morphology is toroidal, while at rates above 0.04 mA/cm^2 thin film growth dominates. A transition from toroidal to thin film morphologies is seen between these two rates. Horstmann et al.[33] formulated a theory based on phase field modeling to account for the current density dependent morphology change. Based on the above discovery and the results obtained by Viswanathan et al.,[28] a scenario of Li_2O_2 thin film deposition and electron-limited electrochemistry can be envisaged for normal and large discharge current densities ranging from 0.1 mA/cm^2 to 1 mA/cm^2.

We present here a multiscale model for LAB, describing the following mechanisms (Fig. 1 with the schematics of the cell):

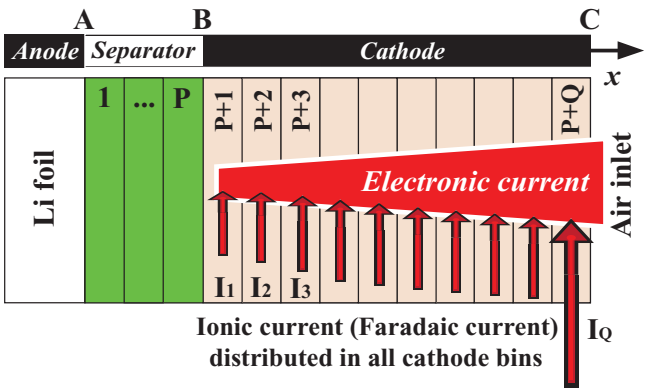

Figure 1. Finite different scheme in modeling the lithium air battery. During discharge, the ionic current is gradually transformed into electronic current from bin #P+1, which is close to the separator, to bin #P+Q, which is close to the air inlet. Therefore, the electronic current is the smallest in bin #P+1 but largest in bin #P+Q. Since oxygen is most easily obtained at bin #P+Q, the faradaic current density is also the highest in that bin.

*Electrochemical Society Active Member.
[z]E-mail: alejandro.franco@u-picardie.fr

- transport of O_2 across the cathode thickness,
- uniform Li_2O_2 thin film growth rate at the same macroscopic location of the cathode,
- existence of a maximum Li_2O_2 thickness due to electron tunneling limit; or an Ohmic resistance for Li_2O_2 thin films, without tunneling restriction.

Note that our approach does not aim at a solution-based ORR kinetics. In that case different models should apply, which requires a detailed investigation into the Li_2O_2 crystallization mechanism in the solution.

Our paper is organized as follows. First we present the mathematical description of our model in the continuum scale. Subsequently, the microscale discharge product morphology is discussed and embedded in the model. Then, we carry out simulations on two cathodes with different PSDs and discuss results in relation to experimental knowledge. Finally we conclude and indicate further direction of our work.

Model Description: Electron Tunneling-Limited

For solving the transport processes, a finite difference scheme is explicitly used through a one-dimensional approach, where the cathode is divided into several "bins" as shown in Fig. 1. A bin is a macroscopic volume element, but its dimension is still small enough to assign a single value for oxygen concentration.

Oxygen transport.— The transport of O_2 is characterized by Fick's diffusion with spatially-distributed ORR kinetics following

$$\frac{\partial c}{\partial t} = \frac{\partial}{\partial x}\left[D\left(\frac{\partial c}{\partial x}\right)\right] - \frac{a j_{\text{Far}}}{nF} \quad [1]$$

where c is the local O_2 concentration, a is the specific surface area, j_{Far} is the faradaic current density due to the reaction

$$2Li^+ + 2e^- + O_2 \rightarrow Li_2O_2$$

$n = 2$ is the number of electrons involved in the above reaction, F is the Faraday constant, and the diffusion coefficient D in the porous electrode is calculated by

$$D = \left(\frac{\epsilon}{\tau}\right) D_0 = \epsilon^{1.5} D_0 \quad [2]$$

In Eq. 2, ϵ is the local porosity and

$$\tau = \frac{1}{\sqrt{\epsilon}} \quad [3]$$

represents a tortuosity correction. At the boundary outside the air inlet, however, we assume merely porosity correction to the O_2 diffusion coefficient, without consideration of tortuosity. The reason lies in the absence of tortuosity for O_2 flowing to boundary C in Fig. 1, but the porosity will influence the rate of O_2 dissolution at that point.

Since the porosity will evolve over time due to Li_2O_2 generation, we define a parameter s called saturation:

$$s \equiv \frac{V_{Li_2O_2}}{\epsilon_0 V} \quad [4]$$

where ϵ_0 is the initial porosity before discharge, $V_{Li_2O_2}$ is the volume of Li_2O_2 in the bin and V is the total volume of the bin. The saturation is obtained by integrating the faradaic current locally:

$$s = \frac{M_{Li_2O_2}}{\epsilon_0 nF \rho_{Li_2O_2}} \int a j_{\text{Far}} dt \quad [5]$$

where $M_{Li_2O_2}$ and $\rho_{Li_2O_2}$ are the molar mass and mass density of Li_2O_2, respectively.

The saturation impacts the porosity ϵ following

$$\epsilon = (1 - s)\epsilon_0 \quad [6]$$

The boundary condition for oxygen transport at the anode/separator interface (point A in Fig. 1) is a Neumann condition

$$N = -D\frac{\partial c}{\partial x} = 0 \quad [7]$$

while at the air inlet (point B in Fig. 1), the boundary condition is a Dirichlet type

$$c = c_{sat} \quad [8]$$

where c_{sat} is the saturated oxygen concentration in the electrolyte when it is exposed to air or pure O_2 at atmospheric pressure. The numerical scheme for solving the O_2 transport is presented in the Appendix section.

Electrode kinetics and the overpotential.— The faradaic current density is assumed to follow a Tafel kinetics

$$j_{\text{Far}} = nFkc^{1-\beta} \exp\left(-\frac{\beta nF\eta}{RT}\right) \quad [9]$$

where k is the kinetic rate, β is the charge transfer coefficient and η is the Tafel overpotential. Since the current rate in a LAB cannot be very high, we neglect the solution phase potential difference in the cathode region, while the solid phase potential within the cathode particles is homogeneous due to their high electronic conductivity. Hence, η will be treated as homogeneous in all the cathode bins.

In carrying out the finite difference method, the separator is divided into P bins, while the cathode is divided into Q bins. In each bin, the total faradaic current is

$$I_i = a_i V_i j_{\text{Far,i}} = a_i A \Delta x j_{\text{Far,i}} \quad [10]$$

where A is the gross cell area and Δx is the thickness of the bin along the x direction in Fig. 1. The total current I is distributed in all the bins, such that the macroscopic current density J is expressed as

$$J = \frac{I}{A} = \frac{1}{A}\sum_i I_i = \sum_i a_i \Delta x j_{\text{Far,i}} \quad [11]$$

where as a first approximation we have neglected the electrochemical double layer charging/discharging current.[34] Combining Eqs. 9 and 11 yields

$$\eta = -\frac{RT}{\beta nF} \ln\left(\frac{J}{\sum_i n a_i \Delta x F k c^{1-\beta}}\right) \quad [12]$$

The cell potential is obtained from the overpotential in Eq. 12, through

$$U = U_0 + \eta - J R_s \quad [13]$$

where R_s is the series resistance per unit cell area.

In Eq. 13 we assume for the equilibrium potential

$$U_0 = 2.96\ V \quad [14]$$

for a LAB with Li anode. Nevertheless, several parameters in Eq. 12 are subject to evolution over time, which requires coupling to the microscale models.

Microscopic parameter evolution.— According to Eq. 12, either the depletion of oxygen or the degradation of active surface area would lead to a larger magnitude of overpotential during discharge. The sudden "death" (sharp drop of cell voltage) of a LAB during galvanostatic discharge may be attributed to two reasons: (i) insufficient oxygen concentration to sustain the required current; (ii) unavailable or insufficient active area to sustain the required current.

The real mechanism for "cell death" in LAB has been a subject of controversies. When presenting the first non-aqueous LAB, Abraham and Jiang[1] pointed out that the end of discharge is probably caused by choking of the pores by the discharge products. Lu et al. demonstrated a toroidal Li_2O_2 morphology, with large particles of even 350 nm diameter seen.[35] Accepting that pure Li_2O_2 crystal is

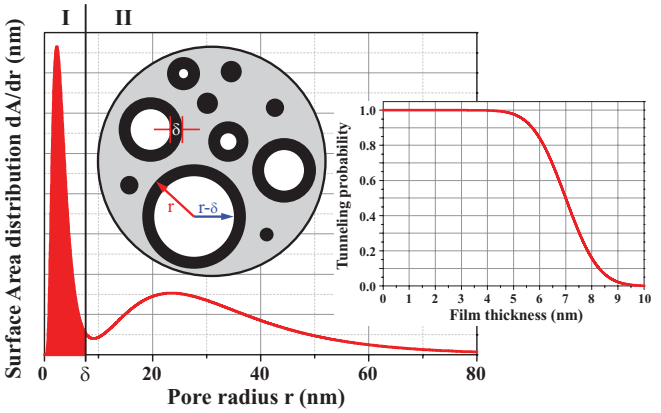

Figure 2. A typical surface area distribution function. Round inset: the clogged pores as well as unclogged pores with surface area modification by the finite thin film thickness δ. Right inset: the electron tunneling probability function versus Li_2O_2 film thickness adopted in this work.

an insulator with 4.81–6.37 eV calculated bandgap,[36–38] the capability of electrons transporting through more than 100-nm-thick Li_2O_2 cannot be explained by a tunneling effect. One approach to get rid of this paradox is to assume that the discharge product is defective Li_2O_2, enabling a bulk conduction mechanism. Therefore, Radin et al.[38,39] examined various surfaces of Li_2O_2 and found that the energetically favorable Li_2O_2 {0001} surface is oxygen rich, which demonstrated a half-metal characteristic. However, Viswanathan et al.[28] showed through experiments and calculations that the poor electronic conductivity of Li_2O_2 is the reason of cell death in LAB. They estimated the maximum tunneling length of electrons to be 5–10 nm. Another explanation could be that the 350 nm diameter toroidal Li_2O_2 particles emerge as discharge product because the reaction mechanism is a solution-based one. On the other hand, once the surface-based mechanism dominates, which is also our interest in this model, we assume electrons may at most tunnel through the Li_2O_2 film for 5–10 nm thickness.

As shown in Fig. 1, each bin is a microscopically large region, such that the critical tunneling range may be dispersed between 5 nm and 10 nm. Instead of uniform distribution, we adopt a normal distribution centered at 7 nm with a width of 2 nm. The tunneling probabilities with various Li_2O_2 thicknesses are demonstrated in the inset of Fig. 2. For those surface area covered by Li_2O_2 thinner than the tunneling range, the resistance is taken as approximately zero. On the other hand, once the local Li_2O_2 thickness is beyond the electron tunneling range, the surface area will be regarded as inactive. Hence, the specific active surface area of a bin covered uniformly by a δ nm-thick Li_2O_2 layer is

$$a_i = \left[\frac{1 - erf(\delta - 7)}{2}\right] a_i^0 \qquad [15]$$

where a_i^0 is the corresponding effective specific surface area without considering electron tunneling limitation. During simulation the Li_2O_2 thickness is updated through

$$\frac{d\delta_i}{dt} = \frac{M_{Li_2O_2} j_{Far,i}}{nF\rho_{Li_2O_2}} \qquad [16]$$

Equation 15 implies that no surface area remains active if the Li_2O_2 thickness exceeds 10 nm. On the other hand, the Li_2O_2 thin film growth scenario also modifies a_i^0 in a geometric way. It is shown in Fig. 2 that any spherical pore with radius less than δ nm will lose all of its surface area due to whole pore choking. In addition, the remaining larger pores also suffer a decrease of surface area, since the effective radius is no longer r, but (r-δ).

The surface area distribution is related to the pore volume distribution $d\bar{V}(r)/dr$ (also named PSD) that can be measured experimentally. Here $\bar{V}(r)$ is the volume percentage of all pores with radius not exceeding r. Assuming spherical pores, one has

$$\frac{dA}{dr} = 4\pi (r-\delta)^2 \frac{d\mathcal{N}}{dr} = \left[\frac{3(r-\delta)^2}{r^3}\right] \frac{d\bar{V}}{dr} \qquad [17]$$

where $d\mathcal{N}/dr$ is the number density distribution of pore sizes. The PSD of some carbon blacks can be mathematically described by a bimodal log-normal distribution function[21,40]

$$\frac{d\bar{V}}{dr} = \frac{1}{\sqrt{\pi}(\ln s_1 + \chi \ln s_2) r} \left\{ \exp\left[-\left(\frac{\ln(r/r_1)}{\ln s_1} \right)^2 \right] + \chi \exp\left[-\left(\frac{\ln(r/r_2)}{\ln s_2} \right)^2 \right] \right\} \qquad [18]$$

where r_1 and r_2 indicate the peak positions of primary and secondary pores, respectively; s_1 and s_2 control peak widths; χ represents the volume ratio of secondary to primary pores.

We assumed two bimodal PSD functions to imitate Ketjen Black and Super P, as plotted in Fig. 3a with parameters given. The geometrically active surface area versus film thickness is plotted in Fig. 3b, with or without the physical tunneling limitation. As the film thickness is below 5 nm, the tunneling limitation has no effects, and the active surface area of Ketjen Black degrades much faster than Super P. This is because in such a thickness range, small pores are more subject to choking and geometric surface area decrease. On the other hand, once the film thickness exceeds 5 nm, tunneling limitation will sharply decrease the active surface area (solid line compared with dashed line). We highlight here that other electrode materials could provide similar structural properties, and our discussions here are general, not limited to carbon.

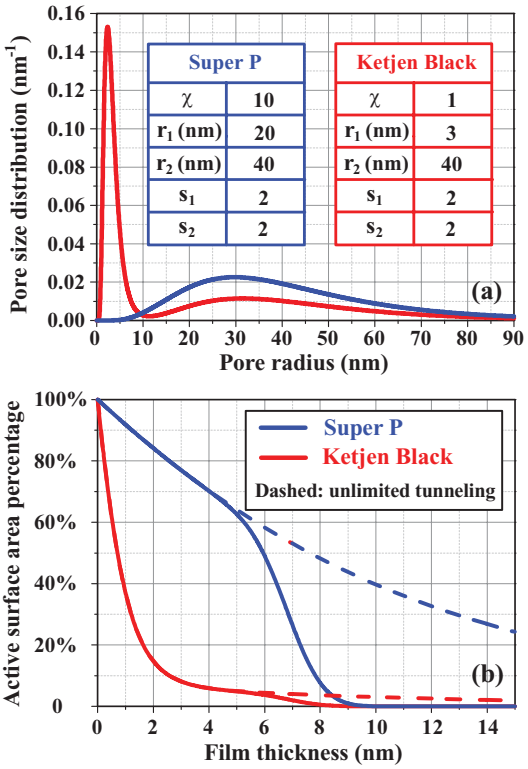

Figure 3. (a) PSD of Super P and Ketjen Black carbons, with parameters in the bimodal distribution function. (b) Percentage of active porous electrode surface area with various Li_2O_2 thin film thicknesses for both Super P (blue) and Ketjen Black (red). The dashed curves represent the raw active surface area percentage without consideration of electron tunneling distance limitation.

A Comparative Linear Resistance Model

Since some groups reported conductive Li_2O_2 surfaces[39] or grain boundaries[41] from first-principles calculation, it is also necessary to consider an alternative picture: that Li_2O_2 is a bulk conductor, whose resistance is dependent on the film thickness. This is an assumption in the LAB models available in the literature,[25] and may be related to the deviation from perfect stoichiometry or perfect single-crystal phase. Our model within this picture is very similar to the tunneling-limited model, except for Eqs. 9, 12 and 15. First, since not all overpotential is relevant to the Tafel kinetics, but some part of the overpotential is consumed by the Li_2O_2 resistance, Eq. 9 should be rewritten as

$$j_{\text{Far}} = nFkc^{1-\beta} \exp\left[-\frac{\beta nF\left(\eta - j_{\text{Far}}R_{\text{Li}_2\text{O}_2}\right)}{RT}\right] \quad [19]$$

where

$$R_{\text{Li}_2\text{O}_2} = \varrho_{\text{Li}_2\text{O}_2}\delta \quad [20]$$

is the specific resistance of the Li_2O_2 thin film, for which we assume a linear dependence on the film thickness. Equation 19 is a transcendental equation on j_{Far} which has to be solved for each bin. However, in finite difference method one can approximately use the j_{Far} and δ values at the last time step for the right hand side. Let $j^{\text{j}}_{\text{Far,i}}$ denote the value of j_{Far} in bin #*i* at discrete time *j*, and the discretized version of Eq. 19 becomes

$$j^{\text{j}}_{\text{Far,i}} = nFk\left(c^{\text{j}}_{\text{i}}\right)^{1-\beta} \exp\left[-\frac{\beta nF\left(\eta - j^{\text{j-1}}_{\text{Far,i}}\varrho_{\text{Li}_2\text{O}_2}\delta^{\text{j-1}}_{\text{i}}\right)}{RT}\right] \quad [21]$$

Equation 21 together with Eq. 11 gives

$$\eta^{\text{j}} = -\frac{RT}{\beta nF}\ln\left[\frac{J}{\sum_i na^{\text{j}}_{\text{i}}\Delta xFk\left(c^{\text{j}}_{\text{i}}\right)^{1-\beta}\exp\left(\frac{\beta nF\varrho_{\text{Li}_2\text{O}_2}j^{\text{j-1}}_{\text{Far,i}}\delta^{\text{j-1}}_{\text{i}}}{RT}\right)}\right] \quad [22]$$

On the other hand, the electron tunneling limit is removed thus Eq. 15 is simply revised to be

$$a_i = a_i^0 \quad [23]$$

while the geometric surface area degradation is still accounted for in a_{i}^0.

Simulation and Discussions

Galvanostatic discharges were simulated for LABs with such two carbon blacks as the cathode material, with the same initial porosity of 0.75. The role of Li^+ in the electrode kinetics is neglected, because Li^+ transport is not a limiting factor and Li^+ concentration is much larger than dissolved O_2 concentration. In this work no electrolyte decomposition is considered, since this could be achieved with stable electrolytes or with proper cathode materials not degrading the electrolyte. If electrolyte decomposition occurs, the most typical reaction product, Li_2CO_3, is a tough insulator with larger bandgap than Li_2O_2.[42] In that case we either need to enhance the relative probability of short electron tunneling ranges like 5 nm in the tunneling model, or to increase the product resistivity in the linear resistance model. A resistance of 0.015 $\Omega \cdot m^2$ is assumed in series, which mainly comes from the electrolyte solution and the solid-electrolyte interphase on the anode. The anode is Li foil while its overpotential is neglected. For the linear resistance model, the resistivity of Li_2O_2 is assumed to be 10^8 $\Omega \cdot m$. Other parameters used in the simulation can be found in the Nomenclature section.

Discharge comparison between the two models.— Figure 4 shows the discharge curves of both Super P and Ketjen Black cells, at various discharge rates. In particular, the tunneling-limited model and the linear resistance model are compared. A great difference is manifested between the two theories regarding the shape of the voltage-discharge capacity curves. The tunneling-limited model shows a long plateau plus a sharp decrease of cell voltage, but a gradually voltage decrease is found in the linear resistance model. In the literature both two shapes have been reported experimentally, for example the tunneling-limited model predicts discharge curves similar to that of Laoire et al.,[43] and Adams et al.,[32] where a relatively stable discharge plateau is followed by a sharp turning point of cell voltage, typically due to a short of reactants or active surface area;[44] while the linear resistance curve shape is close to Yang et al.,[45] and Viswanathan et al.,[29] where a gradual decrease of cell voltage is seen during discharge, indicating an increasing resistance in series. Indeed, it is possible that some of these experiments were in the solution phase reaction mode, but at high discharge rates both of the two I-V shapes are also seen. For example, Laoire et al.[43] used up to 0.25 mA/cm^2 rate, while Yang et al.[45] used up to 0.5 mA/cm^2 rate.

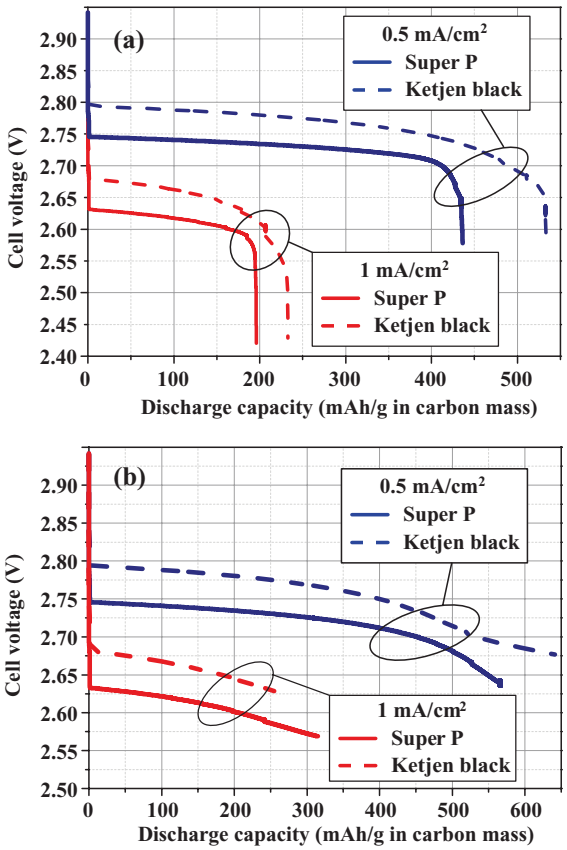

Figure 4. Comparison of simulated galvanostatic discharge curves for LABs with Super P and Ketjen Black as the cathode material. The discharge current rate is either 0.5 mA/cm^2 (blue curves) or 1 mA/cm^2 (red curves). Simulated by: (a) Electron tunneling-limited model; (b) linear resistance model.

Notwithstanding the difference in the discharge curve shape, there are many common features between the two theories, with regard to the influence of carbon PSD. For both theories, cells with Ketjen Black carbon have higher cell potential, because its specific surface area is larger than Super P. At the same macroscopic current density, the actual current density at the porous electrode surface is much smaller for a high surface ratio material.

In reality, electron tunneling and Ohmic conductance may coexist. As the film thickness is less than 5 nm, electron tunneling could dominate. However, as some parts of the surface area are covered by a thick Li_2O_2 film and thus regarded as "inactive" in the tunneling sense, electrons may still transport through them with a very high resistance. The linear Li_2O_2 resistance model is implemented here merely for comparison purposes. In the following sections we shall only focus on the electron tunneling-limited theory.

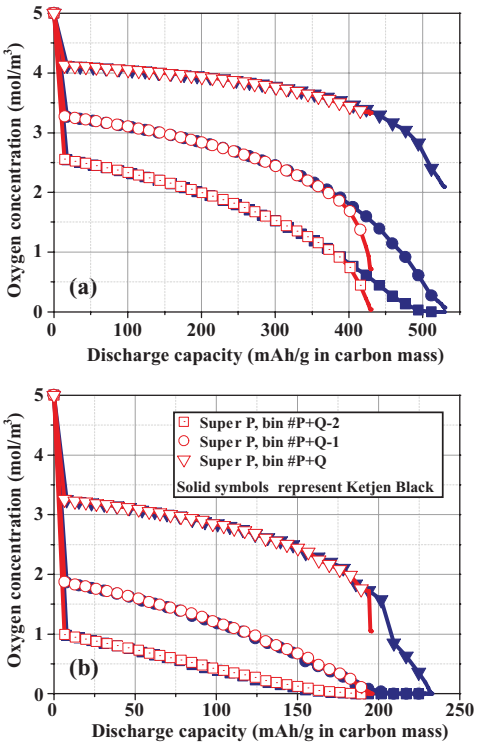

Figure 5. Comparison of oxygen concentration in the last three bins (bin #P+Q is the one close to air inlet) for LABs with Super P and Ketjen Black as the cathode material, simulated within the tunneling-limited model. The discharge current rate is either (a) 0.5 mA/cm^2 or (b) or 1 mA/cm^2. Characteristic markers for various curves in (a), while not shown, is the same as in (b).

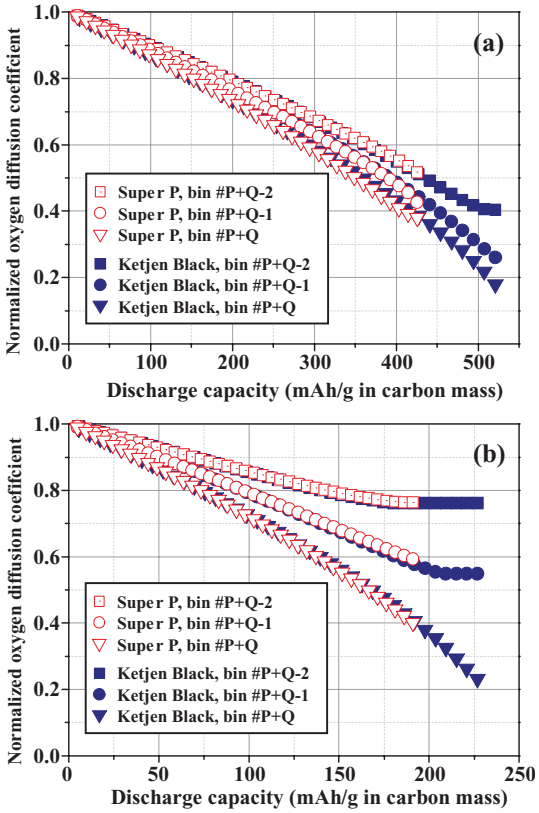

Figure 6. Comparison of oxygen diffusion coefficient evolution for Super P and Ketjen Black cells discharged at (a) 0.5 mA/cm^2; (b) 1 mA/cm^2, simulated within the tunneling-limited model. For each cell, bin #P+Q is the first bin close to the air inlet. The initial oxygen diffusion coefficient (homogeneous for all over the cathode) is normalized to 1.0.

Oxygen concentration profile.— Before discharge, the oxygen concentration in the electrolyte is homogeneous, assumed to be 5 mol/m^3 in all bins. During discharge, the oxygen concentrations in those bins close to the separator drop sharply due to the consumption by faradaic current. No oxygen can be afforded from the Li foil, but the only oxygen diffusion pathway is from the air inlet at bin #P+Q. Figure 5 demonstrates the evolution of oxygen concentration in the last three bins during 0.5 mA/cm^2 and 1 mA/cm^2 discharge for the tunneling-limited model. The last bin (near the air inlet, #P+Q) is crucial to the performance of LABs since other bins usually suffer from oxygen depletion before the end of discharge. At 0.5 mA/cm^2 rate, the last bin still possesses a considerable amount of oxygen, i.e., more than 2 mol/m^3 in both Super P and Ketjen Black cells. Yet, at 1 mA/cm^2 rate the last bin is out of oxygen at the end of discharge for the Ketjen Black cell, while it shows a sharp drop of oxygen concentration at the end of discharge for the Super P cell. Both cells show oxygen depletion only at high discharge rates. Hence, for better rate capacity it is significant to improve the amount of oxygen in the cathode, where the key is to resolve the transport blockage problem near the air inlet.

Discharge capacity.— High available surface area is important since it leads to less overpotential during discharge. Nevertheless, that a high surface area leads to larger discharge capacity is not straightforward. To gain more insights into why Ketjen Black exhibits more discharge capacity, the evolution of oxygen diffusion coefficient and the evolution of active surface area during 0.5 mA/cm^2 discharge are demonstrated in Fig. 6 and Fig. 7, respectively. For both cells, at the end of discharge (436 mAh/g for Super P and 534 mAh/g for Ketjen Black) the oxygen diffusion coefficients show severe but not fatal degradation even for the last bin; instead, the zero active surface area in the last bin clearly signifies the end of discharge (Fig. 7). Hence, Ketjen Black is superior in discharge capacity because it affords more

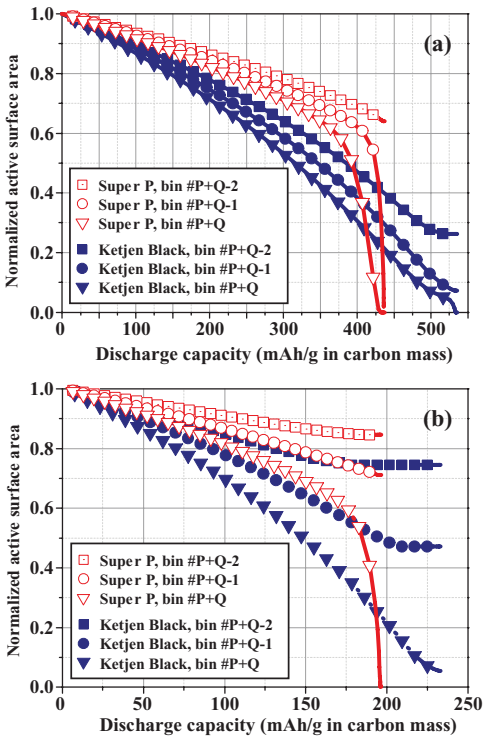

Figure 7. Comparison of active surface area evolution during 0.5 mA/cm^2 discharge for Super P and Ketjen Black cells, simulated within the tunneling-limited model. For each cell, bin #P+Q is the first bin close to the air inlet. The initial active surface area (homogeneous for all over the cathode) is normalized to 1.0.

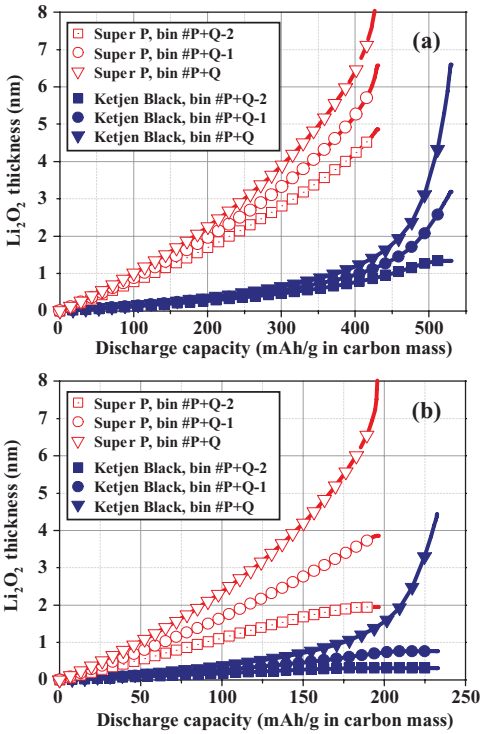

Figure 8. The thicknesses of Li_2O_2 thin films in different bins (bin #P+Q is the one close to air inlet) during the discharge process for both Super P and Ketjen Black cells, simulated within the tunneling-limited model. Discharge current densities are: (a) 0.5 mA/cm^2; (b) 1 mA/cm^2.

active surface area, while the oxygen transport is still not fully blocked. A detailed comparison between Fig. 3b and Fig. 7 appears to be contradictive. Indeed, the percentage of active surface area is higher in Super P than in Ketjen Black for most Li_2O_2 film thickness values, because Super P mainly consists of large secondary pores. Yet, the Li_2O_2 thin film growth rates are different in the two carbons. We plot in Fig. 8 the Li_2O_2 thickness evolution in the last three bins, during the discharge procedure. For both Super P and Ketjen Black cells, the Li_2O_2 thickness distribution is highly inhomogeneous, while the last bin has the fastest Li_2O_2 growth rate. Moreover, the Super P cell has faster growth rate than Ketjen Black since at the same Li_2O_2 volume, the thickness is inversely proportional to the surface area. Hence, electron tunneling limit occurs earlier in Super P than in Ketjen Black. To sum up, there is a compromise between specific surface area and tolerance of pore choking. Regarding the former small pores are preferred, while for the latter large pores or mesopores are preferred.

Conclusions and Perspectives

In this paper we have proposed a multiscale model for non-aqueous LABs at medium and high discharge rates, where the morphology of Li_2O_2 is thin film covering the active cathode particles. There are three active surface area degradation mechanisms according to the electron tunneling-limited scenario: (i) geometric pore surface area decrease due to the finite film thickness; (ii) pore fully occupied by discharge products; (iii) film thickness beyond the tunneling range of electrons. For the latter two mechanisms the pore will lose all its active surface area. Simulation on two LABs with Super P and Ketjen Black carbons reveals different key points regarding discharge capacity and rate performance. On the one hand, the end of galvanostatic discharge is caused by unavailable active surface area near the air inlet, rather than the blockage of oxygen transport. Ketjen Black cell shows larger discharge capacity because the Li_2O_2 growth rate is low, thanks to the high specific surface area. A compromise between high surface area (small pore size) and slow degradation rate of active surface (large pore size) has been demonstrated. On the other hand, oxygen concentration is more relevant to the rate performance of LABs.

A comparative simulation is also done by assuming a linear Ohmic resistance for the Li_2O_2 thin film. In this case, the voltage decreases gradually during discharge, different from the tunneling-limited theory where a long discharge plateau is followed by a sudden voltage drop. Our multiscale simulation framework allows either of the two resistance models for Li_2O_2. It is also highly probable that these two pictures co-exist, the modeling of which is our future interest. However, in any case the microstructure of the cathode influences the cell performance significantly, such that a multiscale model is mandatory for correct interpretation of experimental results. Our microstructurally based approach can also be extended to fuel cells and supercapacitor modeling, as we have recently demonstrated.[46]

Acknowledgments

Prof. Dominique Larcher at LRCS and Dr. Lee Johnson at University of St. Andrews are gratefully acknowledged for helpful discussions. The support of Prof. Jean-Marie Tarascon (Collège de France, Paris) and Dr. Mathieu Morcrette at LRCS is greatly appreciated.

Appendix A: Numerical Schemes

The models are implemented within the in-house LRCS computational approach MS LIBER-T.[47]

We use a forward-time finite difference scheme in solving the oxygen balance equation:

$$c_i^{j+1} = r\left(\epsilon_i^j\right)^{1.5} c_{i-1}^j + \left\{1 - r\left[\left(\epsilon_i^j\right)^{1.5} + \left(\epsilon_{i+1}^j\right)^{1.5}\right]\right\} c_i^j + r\left(\epsilon_{i+1}^j\right)^{1.5} c_{i+1}^j \quad [A1]$$

for each separator bin and

$$\begin{aligned} c_i^{j+1} &= r\left(\epsilon_i^j\right)^{1.5}\left(1-s_i^j\right)^{1.5} c_{i-1}^j \\ &+ \left\{1 - r\left[\left(\epsilon_i^j\right)^{1.5}\left(1-s_i^j\right)^{1.5} + \left(\epsilon_{i+1}^j\right)^{1.5}\left(1-s_{i+1}^j\right)^{1.5}\right]\right\} c_i^j \\ &+ r\left(\epsilon_{i+1}^j\right)^{1.5}\left(1-s_{i+1}^j\right)^{1.5} c_{i+1}^j - \frac{\Delta t a_i^j}{nF} j_{\mathrm{Far,i}}^j \end{aligned} \quad [A2]$$

for each cathode bin. The generic form A_i^j represents the value of A at bin #i at time j. The unit-less parameter r is defined as

$$r = D_0 \frac{\Delta t}{\Delta x^2} \quad [A3]$$

where Δt and Δx are the time interval and the width of each bin, respectively.

The boundary conditions are specified explicitly as

- Boundary A

$$c_1^{j+1} = \left[1 - r\left(\epsilon_1^j\right)^{1.5}\right] c_1^j + r\left(\epsilon_2^j\right)^{1.5} c_2^j \quad [A4]$$

- Boundary B

$$\begin{aligned} c_P^{j+1} &= r\left(\epsilon_P^j\right)^{1.5} c_{P-1}^j + \left\{1 - r\left[\left(\epsilon_P^j\right)^{1.5} + \left(\epsilon_{P+1}^j\right)^{1.5}\left(1-s_{P+1}^j\right)^{1.5}\right]\right\} c_P^j \\ &+ r\left(\epsilon_{P+1}^j\right)^{1.5}\left(1-s_{P+1}^j\right)^{1.5} c_{P+1}^j \end{aligned} \quad [A5]$$

$$\begin{aligned} c_{P+1}^{j+1} &= r\left(\epsilon_{P+1}^j\right)^{1.5}\left(1-s_{P+1}^j\right)^{1.5} c_P^j \\ &+ \left\{1 - r\left[\left(\epsilon_{P+1}^j\right)^{1.5}\left(1-s_{P+1}^j\right)^{1.5} + \left(\epsilon_{P+2}^j\right)^{1.5}\left(1-s_{P+2}^j\right)^{1.5}\right]\right\} c_{P+1}^j \\ &+ r\left(\epsilon_{P+2}^j\right)^{1.5}\left(1-s_{P+2}^j\right)^{1.5} c_{P+2}^j - \frac{\Delta t a_{P+1}^j}{nF} j_{\mathrm{Far,P+1}}^j \end{aligned} \quad [A6]$$

- Boundary C

$$\begin{aligned} c_{P+Q}^{j+1} &= r\left(\epsilon_{P+Q}^j\right)^{1.5}\left(1-s_{P+Q}^j\right)^{1.5} c_{P+Q-1}^j \\ &+ \left\{1 - r\left[\left(\epsilon_{P+Q}^j\right)^{1.5}\left(1-s_{P+Q}^j\right)^{1.5} + \underline{\epsilon_{P+Q}^j\left(1-s_{P+Q}^j\right)}\right]\right\} c_{P+Q}^j \\ &+ \underline{r\epsilon_{P+Q}^j\left(1-s_{P+Q}^j\right)} c_{sat} - \frac{\Delta t a_{P+Q}^j}{nF} j_{\mathrm{Far,P+Q}}^j \end{aligned} \quad [A7]$$

Notice that outside boundary C, we only applied porosity correction to the diffusion coefficient, but not the tortuosity correction. This corresponds to the physical situation that no tortuosity is found for the air flow from outside the cell. However, for oxygen to dissolve into the out-most part of the cathode, the porosity there does play a role, as demonstrated by the underlined terms in Eq. A7.

Appendix B: Calculation of the specific discharge capacity

We assume that the composite cathode consists of carbon and binder (typically PTFE) in a mass ratio μ:1. At a galvanostatic discharge current density of J, if the cell stops discharging at time t, the specific discharge capacity C in carbon mass at this rate is

$$C = \frac{Jt(\mu\rho_B + \rho_C)}{(3.6 \times 10^6)\mu\rho_B\rho_C L_{cat}} \quad [B1]$$

where the units of all variables are indicated in the Nomenclature.

List of Symbols and Parameter Values Used in Simulations

Symbol	Parameter name	Unit	Value used
a	Specific surface area	m^{-1}	
$a_{KB,0}$	Specific surface area of Ketjen Black	m^{-1}	4.54×10^8
$a_{SP,0}$	Specific surface area of Super P	m^{-1}	6.87×10^7
A	Cell area	m^2	
c	O_2 molar concentration	$mol \cdot m^{-3}$	
c_{sat}	Saturated O_2 molar concentration	$mol \cdot m^{-3}$	5
C	Specific discharge capacity in carbon mass	$mAh \cdot g^{-1}$	
D	Diffusion coefficient	$m^2 \cdot s^{-1}$	
D_0	O_2 diffusion coefficient	$m^2 \cdot s^{-1}$	10^{-9}
F	Faraday constant	$C \cdot mol^{-1}$	96485
I	Current	A	
J	Current density	$A \cdot m^{-2}$	
j_{Far}	Microscopic faradaic current density	$A \cdot m^{-2}$	
k	Kinetic rate	$mol^{0.5} \cdot m^{-0.5} \cdot s^{-1}$	5×10^{-12}
L_{cat}	Cathode thickness	m	7.5×10^{-4}
L_{sep}	Separator thickness	m	7.5×10^{-5}
n	Number of electrons involved in the elementary cathodic reaction	-	2
M	Molar mass	$g \cdot mol^{-1}$	
$M_{Li_2O_2}$	Li_2O_2 Molar mass	$g \cdot mol^{-1}$	45.88
N	Flux density	$mol \cdot m^{-2} \cdot s^{-1}$	
P	Number of bins in the separator	-	3
Q	Number of bins in the cathode	-	30
R	Universal gas constant	$J \cdot mol^{-1} \cdot K^{-1}$	8.31
$R_{Li_2O_2}$	Specific resistance of (defective) Li_2O_2	$\Omega \cdot m^2$	
R_S	Series resistance	$\Omega \cdot m^2$	0.015
r	Pore radius (in the main text)	nm	
r	Dimensionless auxiliary parameter in finite difference method	–	
s	Saturation	–	
t	Time	s	
T	Temperature	K	298
U	Cell voltage	V	
U_0	Open circuit potential of the cathode versus Li/Li^+	V	2.96
V	Volume	m^3	
x	1-D spatial coordinate	m	
β	Charge transfer coefficient	-	0.5
δ	Thickness of discharge product	nm	
Δt	Time interval in finite different method	s	
Δx	Width of a bin	m	2.5×10^{-5}
ε	Porosity	-	
ε_{cat}	Cathode porosity	-	0.75
ε_{sep}	Separator porosity	-	1
η	overpotential	V	
μ	Carbon-to-binder mass ratio	-	4
ρ	Density	$g \cdot cm^{-3}$	
ρ_B	Binder density	$g \cdot cm^{-3}$	2.2
ρ_C	Carbon density	$g \cdot cm^{-3}$	1.8
$\rho_{Li_2O_2}$	Li_2O_2 density	$g \cdot cm^{-3}$	2.31
$\varrho_{Li_2O_2}$	Resistivity of (defective) Li_2O_2	$\Omega \cdot m$	10^8
τ	Tortuosity	-	

References

1. K. M. Abraham and Z. Jiang, *J. Electrochem. Soc.*, **143**, 1 (1996).
2. J. Christensen, P. Albertus, R. S. Sanchez-Carrera, T. Lohmann, B. Kozinsky, R. Liedtke, J. Ahmed, and A. Kojic, *J. Electrochem. Soc.*, **159**, R1 (2011).
3. B. D. McCloskey, D. S. Bethune, R. M. Shelby, G. Girishkumar, and A. C. Luntz, *J. Phys. Chem. Lett.*, **2**, 1161 (2011).
4. G. Girishkumar, B. McCloskey, A. C. Luntz, S. Swanson, and W. Wilcke, *J. Phys. Chem. Lett.*, **1**, 2193 (2010).
5. M. Mirzaeian and P. J. Hall, *Electrochimica Acta*, **54**, 7444 (2009).
6. C. Tran, X.-Q. Yang, and D. Qu, *J. Power Sources*, **195**, 2057 (2010).
7. J. Xiao, D. Wang, W. Xu, D. Wang, R. E. Williford, J. Liu, and J.-G. Zhang, *J. Electrochem. Soc.*, **157**, A487 (2010).
8. J. Xiao, D. Mei, X. Li, W. Xu, D. Wang, G. L. Graff, W. D. Bennett, Z. Nie, L. V. Saraf, I. A. Aksay, J. Liu, and J.-G. Zhang, *Nano Lett.*, **11**, 5071 (2011).
9. S. R. Younesi, S. Urbonaite, F. Björefors, and K. Edström, *J. Power Sources*, **196**, 9835 (2011).
10. Z. Peng, S. A. Freunberger, Y. Chen, and P. G. Bruce, *Science*, **337**, 563 (2012).
11. Y.-C. Lu, Z. Xu, H. A. Gasteiger, S. Chen, K. Hamad-Schifferli, and Y. Shao-Horn, *J. Am. Chem. Soc.*, **132**, 12170 (2010).
12. M. M. Ottakam Thotiyl, S. A. Freunberger, Z. Peng, Y. Chen, Z. Liu, and P. G. Bruce, *Nat. Mater.*, **12**, 1050 (2013).
13. M. M. Ottakam Thotiyl, S. A. Freunberger, Z. Peng, and P. G. Bruce, *J. Am. Chem. Soc.*, **135**, 494 (2013).
14. M. J. Trahan, S. Mukerjee, E. J. Plichta, M. A. Hendrickson, and K. M. Abraham, *J. Electrochem. Soc.*, **160**, A259 (2013).
15. W. Walker, V. Giordani, J. Uddin, V. S. Bryantsev, G. V. Chase, and D. Addison, *J. Am. Chem. Soc.*, **135**, 2076 (2013).
16. A. A. Franco, *RSC Adv.*, **3**, 13027 (2013).
17. L. F. L. Oliveira, C. Jallut, and A. A. Franco, *Electrochimica Acta*, **110**, 363 (2013).
18. R. F. de Morais, P. Sautet, D. Loffreda, and A. A. Franco, *Electrochimica Acta*, **56**, 10842 (2011).
19. K. Malek and A. A. Franco, *J. Phys. Chem. B*, **115**, 8088 (2011).
20. A. A. Franco, *PEMFC degradation modeling and analysis, book chapter in: Polymer electrolyte membrane and direct methanol fuel cell technology (PEMFCs and DMFCs)-Volume 1: Fundamentals and performance*, edited by C Hartnig and C. Roth (Woodhead, Cambridge, UK, 2011).
21. A. A. Franco and K.-H. Xue, *ECS J. Solid State Sci. Technol.*, **2**, M3084 (2013).
22. S. S. Sandhu, J. P. Fellner, and G. W. Brutchen, *J. Power Sources*, **164**, 365 (2007).
23. P. Andrei, J. P. Zheng, M. Hendrickson, and E. J. Plichta, *J. Electrochem. Soc.*, **157**, A1287 (2010).
24. P. Albertus, G. Girishkumar, B. McCloskey, R. S. Sánchez-Carrera, B. Kozinsky, J. Christensen, and A. C. Luntz, *J. Electrochem. Soc.*, **158**, A343 (2011).
25. Y. Wang, *Electrochimica Acta*, **75**, 239 (2012).
26. X. Li and A. Faghri, *J. Electrochem. Soc.*, **159**, A1747 (2012).
27. V. Y. Nimon, S. J. Visco, L. C. D. Jonghe, Y. M. Volfkovich, and D. A. Bograchev, *ECS Electrochem. Lett.*, **2**, A33 (2013).
28. V. Viswanathan, K. S. Thygesen, J. S. Hummelshøj, J. K. Nørskov, G. Girishkumar, B. D. McCloskey, and A. C. Luntz, *J. Chem. Phys.*, **135**, 214704 (2011).
29. V. Viswanathan, J. K. Nørskov, A. Speidel, R. Scheffler, S. Gowda, and A. C. Luntz, *J. Phys. Chem. Lett.*, **4**, 556 (2013).
30. C. O. Laoire, S. Mukerjee, K. M. Abraham, E. J. Plichta, and M. A. Hendrickson, *J. Phys. Chem. C*, **114**, 9178 (2010).
31. R. R. Mitchell, B. M. Gallant, Y. Shao-Horn, and C. V. Thompson, *J. Phys. Chem. Lett.*, **4**, 1060 (2013).
32. B. D. Adams, C. Radtke, R. Black, M. L. Trudeau, K. Zaghib, and L. F. Nazar, *Energy Environ. Sci.*, **6**, 1772 (2013).
33. B. Horstmann, B. Gallant, R. Mitchell, W. G. Bessler, Y. Shao-Horn, and M. Z. Bazant, *J. Phys. Chem. Lett.*, **4**, 4217 (2013).
34. A. A. Franco, P. Schott, C. Jallut, and B. Maschke, *J. Electrochem. Soc.*, **153**, A1053 (2006).
35. Y.-C. Lu, D. G. Kwabi, K. P. C. Yao, J. R. Harding, J. Zhou, L. Zuin, and Y. Shao-Horn, *Energy Environ. Sci.*, **4**, 2999 (2011).
36. J. S. Hummelshøj, J. Blomqvist, S. Datta, T. Vegge, J. Rossmeisl, K. S. Thygesen, A. C. Luntz, K. W. Jacobsen, and J. K. Nørskov, *J. Chem. Phys.*, **132**, 071101 (2010).
37. J. M. Garcia-Lastra, J. D. Bass, and K. S. Thygesen, *J. Chem. Phys.*, **135**, 121101 (2011).
38. M. D. Radin, F. Tian, and D. J. Siegel, *J. Mater. Sci.*, **47**, 7564 (2012).
39. M. D. Radin, J. F. Rodriguez, F. Tian, and D. J. Siegel, *J. Am. Chem. Soc.*, **134**, 1093 (2012).
40. M. Eikerling, *J. Electrochem. Soc.*, **153**, E58 (2006).
41. W. T. Geng, B. L. He, and T. Ohno, *J. Phys. Chem. C*, **117**, 25222 (2013).

42. J. M. Garcia-Lastra, J. S. G. Myrdal, R. Christensen, K. S. Thygesen, and T. Vegge, *J. Phys. Chem. C*, **117**, 5568 (2013).
43. C. Ó. Laoire, S. Mukerjee, E. J. Plichta, M. A. Hendrickson, and K. M. Abraham, *J. Electrochem. Soc.*, **158**, A302 (2011).
44. E. J. Nemanick, *J. Power Sources*, **247**, 26 (2014).
45. X. Yang, P. He, and Y. Xia, *Electrochem. Commun.*, **11**, 1127 (2009).
46. S. Strahl, A. Hussar, and A. A. Franco, *Int. J. Hydrogen Energy*, submitted (2013).
47. http://www.modeling-electrochemistry.com.